PROCEEDINGS OF THE ROYAL SOCIETY A

FirstCite® e-publishing

Proc. R. Soc. A
doi:10.1098/rspa.2009.0496
Published online

Linear stability of a solid–vapour interface

By Robert W. Style* and M. Grae Worster

Department of Applied Mathematics and Theoretical Physics, Institute of Theoretical Geophysics, Centre for Mathematical Sciences, University of Cambridge, Wilberforce Road, Cambridge CB3 0WA, UK

We investigate a system consisting of a condensed phase in contact with its vapour. We derive similarity solutions for vapour and temperature profiles and calculate the condition for the presence of vapour supersaturation adjacent to the condensed phase. We analyse the linear stability of a solid–vapour interface with varying atmospheric conditions. The instability is qualitatively similar to the Mullins–Sekerka instability in binary alloys but the results highlight the important parameters for the solid/vapour problem. We derive the neutral stability condition and results are applied to frost flowers, which are small hoar-frost-like crystals that grow on sea ice, and to physical vapour deposition. The results are applicable to many problems in the wide field of condensed-phase/vapour systems.

Keywords: vapour deposition; frost flowers; linear stability

1. Introduction

Processes involving evaporation and condensation are many and varied in both natural and industrial situations. Among many examples of such situations, condensation in controlled environments is important in producing precision crystals and in coating objects with protective films (e.g. Mahan 2000), while natural condensation is responsible for some of the beautiful patterning seen in snow crystals and in jack frost 'ferns' on cold windows (Libbrecht 2005). Similarly, evaporation is important in many processes on many scales, ranging from sea-surface evaporation in meteorology, to coastal weathering by evaporation of saltwater, to pattern production such as seen during evaporation of impure films and coffee drops (Deegan *et al.* 2000; Style & Wettlaufer 2007). In order to fully understand these and other related processes, we need to know the morphological behaviour of a solid/vapour or liquid/vapour boundary based on imposed system boundary conditions such as air temperature and vapour concentration.

In a previous paper, we considered the case of a condensed phase, such as ice or water, in contact with its vapour (Style & Worster 2009). We outlined the relevant equations for the system, and showed that these equations lead to a regime diagram (figure 1) that shows the atmospheric conditions under which different vapour-related phenomena occur (see the caption to figure 1 for further details). In the first part of this paper, we expand upon this work by presenting the

*Author for correspondence (style@maths.ox.ac.uk).

Received 23 September 2009
Accepted 2 November 2009

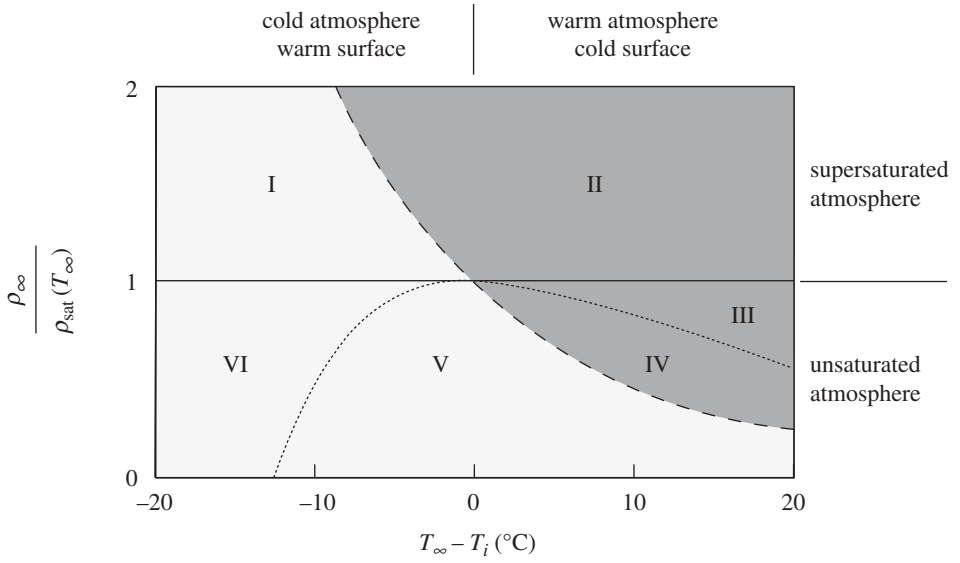

Figure 1. Regime diagram for an ice (water)/vapour system, from Style & Worster (2009). When the relative humidity is above the dashed line (dark grey region), vapour condenses onto the ice (water). Below the dashed line (light grey region), ice (water) evaporates. Above the dash-dotted line there is supersaturation of the vapour immediately above the ice (water). Below the dash-dotted line the air is undersaturated. The continuous horizontal line corresponds to the saturation point of the far-field air where the relative humidity is 100%. Values used are those appropriate to the ice/vapour system.

full equations for a system consisting of a condensed phase in contact with vapour. For the case where there is no ambient flow in the vapour, we find similarity solutions for the temperature and vapour density profiles. These profiles are first used to calculate new conditions separating regimes in the regime diagram in the case that the diffusivities of vapour and heat in the air are not equal. We then use the temperature and vapour density profiles to demonstrate the vapour properties in the different regimes of the regime diagram.

In the second part of this paper, we calculate the linear stability of a solid surface in contact with vapour and its dependence on the atmospheric conditions present in the system. We add to the regime diagram by identifying regions where surface instability occurs. We then apply the results to examples in two distinct regimes. Firstly, we consider the growth of frost flowers in regime VI. These hoar-frost-like crystals grow when a warm ice surface is evaporating into a cold atmosphere. When the atmosphere is sufficiently cold, supersaturation exists above the interface, and the frost flowers grow into this supersaturated layer (Style & Worster 2009). We show that the ice surface is linearly stable for typical frost flower growth conditions and suggest that this means that frost flowers are likely to be formed by heterogeneous nucleation when foreign ice particles land on the surface of the ice. Secondly, we consider the growth of molecularly rough crystals by vapour deposition in regime IV. If morphological instability of the crystal occurs during growth, the resulting physical properties of the crystals

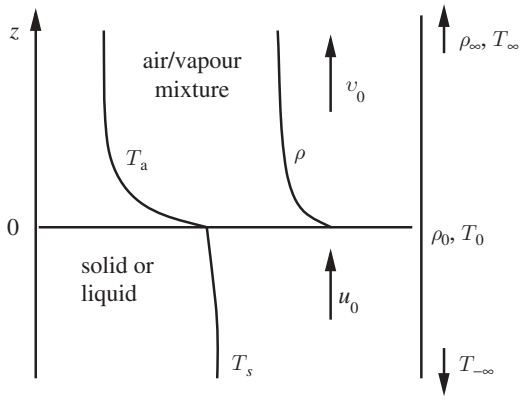

Figure 2. Definition diagram for the model problem. See text for further details.

can be markedly different from the optimal crystal characteristics. Instability has been known to result in undulations on the crystal surface as well as causing multigrain, columnar and dendritic structures to grow (Louchev 1994). We show that, despite the lack of supersaturation above the interface, the majority of this regime is unstable. The analysis shows that crystals can be grown in a stable manner only at very slow growth velocities and we derive a new expression for the maximal stable growth velocity.

2. Temperature and vapour profiles during the evolution of a planar interface

First, we present the equations relevant to a planar system consisting of a condensed phase in contact with its vapour. We solve these equations to obtain the temperature profile in the condensed phase and the vapour and temperature profiles in the air. We choose to model the system as a half plane of pure solid or liquid in contact with a two-component vapour. This vapour comprises a bulk inert gas (such as nitrogen), which we term 'air', and water vapour. Figure 2 illustrates the model and shows variables defined in the text. The water vapour content of the air is characterized by its partial density ρ and diffuses through the air with diffusivity D. This means that the vapour density obeys the advection–diffusion equation

$$\frac{\partial \rho}{\partial t} + v_0 \frac{\partial \rho}{\partial z} = D \frac{\partial^2 \rho}{\partial z^2}, \tag{2.1}$$

where the velocity of air and vapour v_0 is assumed spatially uniform, but time-dependent and $z = 0$ corresponds to the condensed-phase/air interface.

Air temperature T_a and temperature in the condensed phase T_s obey similar advection–diffusion equations,

$$\frac{\partial T_a}{\partial t} + v_0 \frac{\partial T_a}{\partial z} = \kappa_a \frac{\partial^2 T_a}{\partial z^2} \tag{2.2}$$

and

$$\frac{\partial T_s}{\partial t} + u_0 \frac{\partial T_s}{\partial z} = \kappa_s \frac{\partial^2 T_s}{\partial z^2}, \tag{2.3}$$

where κ_a and κ_s are the thermal diffusivities of the air and condensed phases respectively and $u_0(t)$ is the velocity of the condensed phase. We assume that the thermal diffusivity of the vapour–air mixture is a constant, and unaffected by variations in vapour density. This assumption is reasonable as typical vapour densities ρ are substantially smaller than the density of air ρ_a, with $\rho/\rho_\mathrm{a} \approx 5 \times 10^{-3}$. Therefore, the thermal diffusivity is effectively that of pure air.

At the interface, there are three natural conservation equations that we use as boundary conditions. First, from conservation of mass,

$$u_0 \rho_s = v_0 \rho_\mathrm{a}, \tag{2.4}$$

where ρ_s is the density of the condensed phase. For an evaporating system, as the water molecules leave the condensed phase, the volume per molecule increases substantially. Therefore, there must be a flow away from the interface in order to avoid a build up of pressure, the strength of which is described by the conservation of mass (i.e. both air and water vapour in the gaseous phase).

Simultaneously with conservation of mass, we must also have a second boundary condition that describes conservation of water vapour at the interface taking the form

$$D \frac{\partial \rho}{\partial z}(0) - v_0 \rho(0) = -u_0 \rho_s. \tag{2.5}$$

The left-hand side of this equation describes the diffusive and advective contributions from the vapour to the mass transport from the surface, while the right-hand side gives the advective transport towards the surface in the condensed phase.

The third conservation condition is that of heat at the interface. This is given by

$$-\rho_s L u_0 = -k_\mathrm{a} \frac{\partial T_\mathrm{a}}{\partial z}(0) + k_s \frac{\partial T_s}{\partial z}(0), \tag{2.6}$$

where L is the appropriate latent heat of condensation for either the vapour–solid transition or the vapour–liquid transition. Thermal conductivities of air and the condensed phase are given by k_a and k_s, respectively. These are related to the thermal diffusivities by the expression $k_i = \rho_i \kappa_i c_{p_i}$, where i corresponds to air or to the condensed phase and c_p is the specific heat capacity. In this equation, the left-hand side represents the latent heat of condensation corresponding to condensation or evaporation at the interface, while terms on the right-hand side give heat conduction through the air and condensed phase, respectively.

Two remaining boundary conditions at the interface are given by continuity of temperature,

$$T_\mathrm{a}(0) = T_s(0), \tag{2.7}$$

and the Clausius–Clapeyron equation (Wood & Battino 1990), expressing vapour saturation (equilibrium) at the phase interface,

$$\rho(0) = \rho_\mathrm{sat}(\infty) \frac{T_\infty}{T_\mathrm{a}(0)} \exp\left(-\frac{ML}{R} \left[\frac{1}{T_\mathrm{a}(0)} - \frac{1}{T_\infty} \right] \right). \tag{2.8}$$

Here $\rho_{\mathrm{sat}}(\infty)$ is the equilibrium vapour pressure at the far-field temperature T_∞, M is the molar mass of water and R is the gas constant. As with the boundary condition for heat conservation, when we consider water or ice as the condensed phase, we must choose the appropriate latent heat of condensation L.

We close the system by taking the temperature and vapour density in the far-field air to be T_∞ and ρ_∞, respectively, while the far-field temperature in the solid is $T_{-\infty}$.

In order to simplify the equations, we make two assumptions. Firstly, we assume that the interface remains planar during growth. We shall demonstrate later that under certain conditions the interface becomes unstable, but this model is still useful for investigation of the vapour conditions during early stage growth.

Secondly, we assume that the vapour content of the air is very small so that $\rho/\rho_{\mathrm{a}} \ll 1$. As a result, we see that, by use of equation (2.4) in the boundary condition for conservation of water vapour (2.5), the advective contribution from the gas is much smaller than the advective contribution in the condensed phase. Thus the equation for conservation of water can be approximated by

$$D\frac{\partial \rho}{\partial z}(0) + u_0 \rho_s = 0. \tag{2.9}$$

(*a*) *Scaling*

We assume that a similarity solution exists, having a fixed interface temperature T_0. The growth rate of the interface will then be such that $u_0 \propto 1/\sqrt{t}$ (e.g. Worster 2000) and the system can be expressed in terms of the dimensionless similarity variable $\eta = z/\sqrt{2Dt}$. By balancing terms in equation (2.9), we choose to non-dimensionalize velocities as

$$u_0 = \frac{\rho_{\mathrm{sat}}(\infty)}{\rho_s}\sqrt{\frac{D}{2t}}\,\tilde{u} \quad \text{and} \quad v_0 = \frac{\rho_{\mathrm{sat}}(\infty)}{\rho_{\mathrm{a}}}\sqrt{\frac{D}{2t}}\,\tilde{u}. \tag{2.10}$$

The non-dimensionalized field variables are given by

$$\theta_{\mathrm{a}}(\eta) = \frac{T_{\mathrm{a}} - T_\infty}{T_{-\infty} - T_\infty}, \quad \theta_s(\eta) = \frac{T_{-\infty} - T_s}{T_{-\infty} - T_\infty} \quad \text{and} \quad \tilde{\rho}(\eta) = \frac{\rho - \rho_\infty}{\rho_{\mathrm{sat}}(\infty)}, \tag{2.11}$$

so that after non-dimensionalization the governing equations become

$$\tilde{\rho}'' + \tilde{\rho}'(\eta - \epsilon_2 \tilde{u}) = 0, \tag{2.12}$$

$$\theta_{\mathrm{a}}'' + \theta_{\mathrm{a}}'(\eta - \epsilon_2 \tilde{u}) = 0 \tag{2.13}$$

and

$$\theta_s'' + \frac{D}{\kappa_s}\theta_s'(\eta - \epsilon_1 \tilde{u}) = 0, \tag{2.14}$$

while the boundary conditions are

$$\tilde{\rho}(0) = \frac{T_\infty}{T_\infty + \Delta T \theta_{\mathrm{a}}(0)} \exp\left(-\frac{ML}{R}\left[\frac{1}{T_\infty + \Delta T \theta_{\mathrm{a}}(0)} - \frac{1}{T_\infty}\right]\right) - \frac{\rho_\infty}{\rho_{\mathrm{sat}}(\infty)}, \tag{2.15}$$

$$\tilde{\rho}(\infty) = 0, \quad \theta_{\mathrm{a}}(\infty) = \theta_s(-\infty) = 0, \tag{2.16}$$

$$\theta_{\mathrm{a}}(0) + \theta_s(0) = 1, \quad \tilde{\rho}'(0) = -\tilde{u} \tag{2.17}$$

Table 1. Table of typical values for water/air.

constant	value	units	constant	value	units
L	2.5×10^6	$\mathrm{J\,kg^{-1}}$	R	8.3144	$\mathrm{J\,K^{-1}\,mol^{-1}}$
c_{p_a}	9.2×10^2	$\mathrm{J\,K^{-1}\,kg^{-1}}$	κ_a	2×10^{-5}	$\mathrm{m^2\,s^{-1}}$
c_{p_s}	4.4×10^3	$\mathrm{J\,K^{-1}\,kg^{-1}}$	κ_s	6×10^{-7}	$\mathrm{m^2\,s^{-1}}$
M	1.8×10^{-2}	$\mathrm{kg\,mol^{-1}}$	D	2.1×10^{-5}	$\mathrm{m^2\,s^{-1}}$
ρ_a	1.3	$\mathrm{kg\,m^{-3}}$	k_a	2.4×10^{-2}	$\mathrm{W\,m^{-1}\,K^{-1}}$
ρ_0	2.4×10^{-3}	$\mathrm{kg\,m^{-3}}$	k_s	2.4	$\mathrm{W\,m^{-1}\,K^{-1}}$
ρ_s	917	$\mathrm{kg\,m^{-3}}$			

and
$$\epsilon_2 S \frac{D}{\kappa_\mathrm{a}} \tilde{u} = \theta_\mathrm{a}'(0) + \frac{k_s}{k_\mathrm{a}} \theta_s'(0). \tag{2.18}$$

The non-dimensional parameters introduced are the ratio of far-field vapour density to the density of the condensed phase

$$\epsilon_1 = \frac{\rho_\mathrm{sat}(\infty)}{\rho_s}, \quad \epsilon_2 = \frac{\rho_\mathrm{sat}(\infty)}{\rho_\mathrm{a}} \quad \text{and} \quad S = \frac{L}{c_{p_\mathrm{a}} \Delta T}, \tag{2.19}$$

and typical values from table 1 show that $\epsilon_1 \simeq 2.6 \times 10^{-6}$, $\epsilon_2 \simeq 1.8 \times 10^{-3}$ and the Stefan number S takes a value of approximately 250. We have also defined $\Delta T = T_\infty - T_{-\infty}$, which we have taken to be approximately 10 K in the estimates above.

(*b*) *Results*

We can solve equations (2.12)–(2.14) to give

$$\tilde{\rho}(\eta) = \left[\frac{T_\infty}{T_\infty + \Delta T \theta_\mathrm{a}(0)} \mathrm{e}^{-\frac{ML}{R}\left(\frac{1}{T_\infty + \Delta T \theta_\mathrm{a}(0)} - \frac{1}{T_\infty}\right)} - \frac{\rho_\infty}{\rho_\mathrm{sat}(\infty)} \right] \times \frac{\operatorname{erfc}\left((\eta - \epsilon_2 \tilde{u})/\sqrt{2}\right)}{\operatorname{erfc}\left(-\epsilon_2 \tilde{u}/\sqrt{2}\right)}, \tag{2.20}$$

$$\theta_\mathrm{a}(\eta) = \theta_\mathrm{a}(0) \frac{\operatorname{erfc}\left(\sqrt{(D/2\kappa_\mathrm{a})}(\eta - \epsilon_2 \tilde{u})\right)}{\operatorname{erfc}\left(-\sqrt{(D/2\kappa_\mathrm{a})}\epsilon_2 \tilde{u}\right)} \tag{2.21}$$

and
$$\theta_s(\eta) = (1 - \theta_\mathrm{a}(0)) \frac{\operatorname{erfc}\left(\sqrt{(D/2\kappa_s)}(\epsilon_1 \tilde{u} - \eta)\right)}{\operatorname{erfc}\left(\sqrt{(D/2\kappa_s)}\epsilon_1 \tilde{u}\right)}. \tag{2.22}$$

Applying the remaining boundary conditions (2.17)$_2$ and (2.18), we find

$$\epsilon_2 \left[\frac{T_\infty}{T_\infty + \Delta T \theta_\mathrm{a}(0)} \mathrm{e}^{-\frac{ML}{R}\left(\frac{1}{T_\infty + \Delta T \theta_\mathrm{a}(0)} - \frac{1}{T_\infty}\right)} - \frac{\rho_\infty}{\rho_\mathrm{sat}(\infty)} \right] = -G\left(-\frac{\epsilon_2 \tilde{u}}{\sqrt{2}}\right) \tag{2.23}$$

and

$$S = \frac{\theta_a(0)}{G\left(-\sqrt{(D/2\kappa_a)}\epsilon_2\tilde{u}\right)} + \frac{c_{p_s}}{c_{p_a}}\frac{1-\theta_a(0)}{G\left(\sqrt{(D/2\kappa_s)}\epsilon_1\tilde{u}\right)}, \tag{2.24}$$

where

$$G(y) = \sqrt{\pi}\, y e^{y^2}\,\mathrm{erfc}(y). \tag{2.25}$$

As ϵ_1, ϵ_2 are both small, the arguments of the functions $G(y)$ are small, and so we can make the approximation $G(y) \approx \sqrt{\pi}\, y$. Equation (2.24) then becomes

$$\sqrt{\frac{\pi}{2}} S\epsilon_1\tilde{u} = \frac{c_{p_s}}{c_{p_a}}\sqrt{\frac{\kappa_s}{D}}\,[1-\theta_a(0)] - \sqrt{\frac{\kappa_a}{D}}\frac{\epsilon_1}{\epsilon_2}\theta_a(0). \tag{2.26}$$

The coefficients of the left-hand side and the second term on the right-hand side of this expression are both small, while the first term on the right-hand side has a coefficient of $O(1)$. Thus, we surmise that $1-\theta_a(0) \ll 1$, and so we can expand equation (2.23) to give

$$\frac{T_\infty}{T_{-\infty}} e^{-(ML/R)(1/T_{-\infty}-1/T_\infty)}[1 + \Delta T(\theta_a(0)-1)f(T_{-\infty})] - \frac{\rho_\infty}{\rho_{\mathrm{sat}}(\infty)} = \sqrt{\frac{\pi}{2}}\tilde{u}, \tag{2.27}$$

where

$$f(T) = \frac{1}{\rho_{\mathrm{sat}}(T)}\frac{\partial \rho_{\mathrm{sat}}(T)}{\partial T} = \frac{ML}{RT^2} - \frac{1}{T}. \tag{2.28}$$

The function $f(T)$ is the local decay rate of the saturation vapour density curve as a function of temperature T.

For a typical ice–vapour system (see table 1) with $\rho_\infty = \rho_{\mathrm{sat}}(T_\infty) = 2.4 \times 10^{-2}\,\mathrm{kg\,m^{-3}}$, $T_\infty = 283\,\mathrm{K}$ and $T_{-\infty} = 273\,\mathrm{K}$ the linear equations (2.26) and (2.27) are easily solved to find that, to two decimal places, $\theta_a(0) = 0.99$ and $\tilde{u} = 1.03$. Comparison with solutions to the full equations show that the values obtained from the linearized equations are accurate to four decimal places, justifying the linearizing approximations made. As these two values are $O(1)$, these results also justify the earlier scalings and importantly show that the advection terms proportional to u_0 are insignificant because $u_0 \sim \epsilon_2\tilde{u}\sqrt{D/2t}$. For example, in the ice–vapour system $u_0 \sim 6 \times 10^{-6}/\sqrt{t}$, so u_0 can be ignored for all but the smallest timescales. We shall use this result in comparing vapour density profiles for varying ρ_∞ at fixed $T_\infty - T_0$.

(*c*) *Discussion*

In our previous analysis (Style & Worster 2009), we used the assumption that the diffusivity of vapour in air D and the thermal diffusivity of air κ_a were equal in order to derive the regime diagram shown in figure 1. Using the thermal and vapour profiles derived above, it is now possible to derive the regime diagram for the case that $D \neq \kappa_a$.

Condensation will occur at the interface when $\rho_\infty > \rho_0$, where subscript 0 indicates values of variables at the phase interface. Then equation (2.8) shows that condensation will occur when

$$\frac{\rho_\infty}{\rho_{\mathrm{sat}}(\infty)} > \frac{T_\infty}{T_0} \mathrm{e}^{-(ML/R)(1/T_0 - 1/T_\infty)}. \tag{2.29}$$

In the limit that the reduced temperature $\tau = (T_\infty - T_0)/T_\infty \ll 1$, this reduces to the equation

$$\frac{\rho_\infty}{\rho_{\mathrm{sat}}}(\infty) > \mathrm{e}^{-m\tau}, \tag{2.30}$$

which is the same condition as previously found for the occurrence of condensation (Style & Worster 2009).

Supersaturation above the interface will occur when

$$\frac{\partial \rho}{\partial z} > \frac{\partial \rho_{\mathrm{sat}}}{\partial T} \frac{\partial T}{\partial z} \tag{2.31}$$

at the interface (Style & Worster 2009). Using the Clausius–Clapeyron equation (2.8) and the expressions for the vapour and temperature profiles in the air (2.20) and (2.21), we find that the condition for supersaturation to occur at the interface is

$$\frac{\rho_\infty}{\rho_{\mathrm{sat}}(\infty)} > \frac{T_\infty}{T_0} \mathrm{e}^{-(ML/R)(1/T_0 - 1/T_\infty)} \left[1 - \sqrt{\frac{D}{\kappa_\mathrm{a}}} f(T_0)(T_0 - T_\infty) \right], \tag{2.32}$$

where we have also made the assumption that $\epsilon_2 \tilde{u}$ and $\sqrt{(D/\kappa_\mathrm{a})}\epsilon_2 \tilde{u}$ are small. When the reduced temperature τ is small, the condition for supersaturation becomes

$$\frac{\rho_\infty}{\rho_{\mathrm{sat}}(\infty)} > \mathrm{e}^{-m\tau} \left[1 + \tau \left(1 + m\sqrt{\frac{D}{\kappa_\mathrm{a}}} - \sqrt{\frac{D}{\kappa_\mathrm{a}}} \right) \right]. \tag{2.33}$$

It can be seen that this condition reduces to the previously determined condition of Style & Worster (2009) when the diffusivities D and κ_a are equal. This condition demonstrates that the amount of supersaturation above the interface is controlled by two separate factors. Firstly, the nonlinearity of the saturation vapour density curve controls the degree of supersaturation above the interface via the temperature dependence of the $\partial \rho_{\mathrm{sat}}/\partial T$ factor in equation (2.31). It is the only cause of supersaturation in the situation when the diffusivities D and κ_a are equal, such as in the case of an ice/water–vapour system (Style & Worster 2009). However, when the diffusivities D and κ_a are allowed to differ from each other, the resulting difference in the thickness of the thermal and solutal boundary layers above the interface also affects the amount of supersaturation. This is analogous to constitutional supercooling in alloy solidification, where supercooling ahead of a freezing solid can occur owing to a high thermal diffusivity in the liquid relative to the solutal diffusivity (Worster 2000). From equation (2.32) it can be seen that the effect of changing the values of the diffusivities depends upon the temperature difference $\Delta T = T_0 - T_\infty$. When ΔT is positive, increasing the vapour diffusivity D relative to the thermal diffusivity κ_a makes supersaturation more likely above the interface. When ΔT is negative, decreasing the vapour diffusivity relative to the thermal diffusivity makes supersaturation more likely above the interface. The case $\Delta T > 0$ can be thought of as being analogous to a melting binary alloy in the unlikely situation that the thermal diffusivity is small

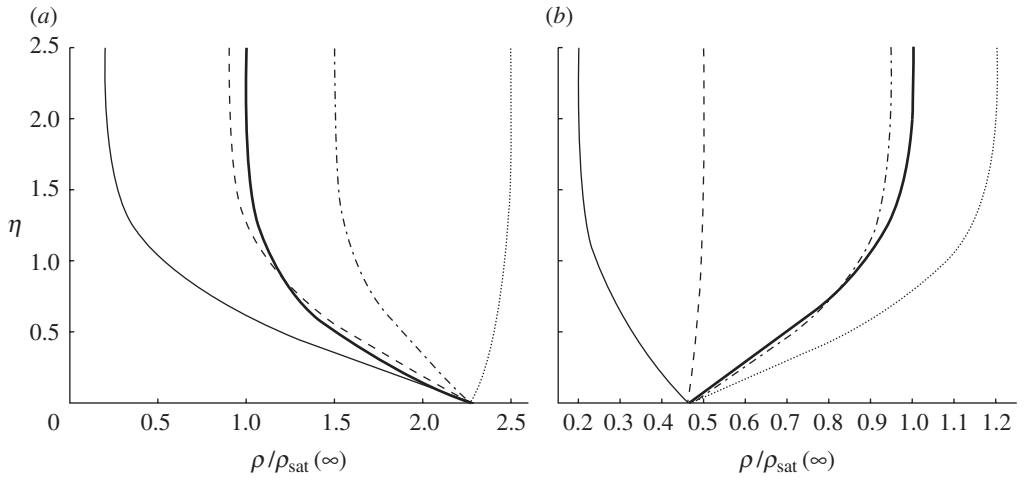

Figure 3. Vapour partial density profiles as a function of the similarity variable η for constant temperature difference $\Delta T = T_\infty - T_0$. $\tilde{u}$ is set to zero. In both (*a*) and (*b*), the thick solid curves show the saturated vapour density corresponding to the air temperature profile. (*a*) $\Delta T = -10\,\mathrm{K}$. Thin solid: regime V, $\rho_\infty/\rho_{\mathrm{sat}}(\infty) = 0.2$. Dashed: regime VI, $\rho_\infty/\rho_{\mathrm{sat}}(\infty) = 0.9$. Dash-dotted: regime I, $\rho_\infty/\rho_{\mathrm{sat}}(\infty) = 1.5$. Dotted: regime II, $\rho_\infty/\rho_{\mathrm{sat}}(\infty) = 2.5$. (*b*) $\Delta T = 10\,\mathrm{K}$. Thin solid: regime V, $\rho_\infty/\rho_{\mathrm{sat}}(\infty) = 0.2$. Dashed: regime IV, $\rho_\infty/\rho_{\mathrm{sat}}(\infty) = 0.5$. Dash-dotted: regime III, $\rho_\infty/\rho_{\mathrm{sat}}(\infty) = 0.95$. Dotted: regime II, $\rho_\infty/\rho_{\mathrm{sat}}(\infty) = 1.2$.

relative to the solutal diffusivity, while the second case is analogous to the typical freezing binary alloy case where the solutal diffusivity is smaller than the thermal diffusivity.

For simplicity, we now return to the case where the thermal and vapour diffusivities in the air are the same so that the vapour conditions above the interface are described by the regime diagram in figure 1. Now, using the error function profiles calculated above, we can illustrate the difference in vapour properties above the condensed phase interface for each regime in figure 1. Figure 3*a*,*b* shows vapour density profiles at fixed $T_\infty - T_0 = 10\,\mathrm{K}$ and $-10\,\mathrm{K}$, respectively. These demonstrate examples of vapour profiles from each of regimes I–VI. By making the assumption that advection in the air is negligible (which we have noted to be appropriate in §2*b*), the temperature profile becomes independent of the relative humidity of the far field. This means that the saturation vapour density profile with respect to ice is invariant for fixed interface and far field temperatures and it is plotted as the thick continuous curve in figure 3*a*,*b*. In figure 3*a*,*b*, each profile is plotted as a function of the similarity variable η (vertical axis) and humidity relative to the far-field saturated vapour density (horizontal axis).

In figure 3*a*,*b*, supersaturation in the vapour occurs when the vapour density is greater than the saturation vapour density (the thick continuous curve). Also condensation onto the interface occurs when the far-field vapour density is greater than the vapour density directly above the interface. Figure 3*a* shows vapour conditions for several different situations with varying far-field densities in the case of a cold, condensed phase in contact with warm air. In this figure,

the thin continuous curve corresponds to regime V where $\rho_\infty/\rho_{\mathrm{sat}}(\infty) = 0.2$, as the vapour density at the phase interface is greater than the vapour density in the far field so evaporation occurs, while no supersaturation occurs at any point above the interface. The dashed line corresponds to vapour conditions in regime IV where $\rho_\infty/\rho_{\mathrm{sat}}(\infty) = 0.5$. Here no supersaturation occurs in the vapour, but the far-field vapour density is greater than the interface density so that condensation occurs. A typical profile for vapour conditions in regime III is given by the dash-dotted line where $\rho_\infty/\rho_{\mathrm{sat}}(\infty) = 0.95$. This regime shows the interesting property that vapour is condensing from an unsaturated far field, but directly above the interface there is a region of vapour supersaturation. Finally in figure 3*a*, the dotted line corresponds to vapour conditions in regime II where $\rho_\infty/\rho_{\mathrm{sat}}(\infty) = 1.2$.

Similar to figure 3*a*, figure 3*b* shows several curves corresponding to different far-field vapour densities, but for the case of a warm condensed phase in contact with cold air. In figure 3*b*, the continuous line corresponds to vapour conditions in regime V where $\rho_\infty/\rho_{\mathrm{sat}}(\infty) = 0.2$. In this case it can be seen that evaporation is occurring from the condensed phase, while there is no supersaturation at any point in the vapour. The dashed line shows the interesting case of vapour growth in regime VI with $\rho_\infty/\rho_{\mathrm{sat}}(\infty) = 0.9$. In this case, there is evaporation from the phase interface into a subsaturated far-field vapour, but there is a region of supersaturation directly above the interface. The dash-dotted line corresponds to vapour conditions in regime I, with $\rho_\infty/\rho_{\mathrm{sat}}(\infty) = 1.55$ where evaporation occurs into a vapour such that the vapour is everywhere supersaturated, and finally the dotted line corresponds to vapour conditions in regime II with $\rho_\infty/\rho_{\mathrm{sat}}(\infty) = 2.5$, where condensation occurs from the vapour and the vapour is entirely supersaturated. It is interesting to note the form of the dashed curve in figure 3*b*. This represents evaporation in regime VI, the regime where we expect frost flowers to grow (Style & Worster 2009). The curve suggests that for a fixed temperature difference between the condensed phase and the air, $T_\infty - T_0$, there is a maximum level of supersaturation that can occur above the interface if the far-field vapour is restricted to being undersaturated (as is found, for instance, in polar regions). If this level of supersaturation is small, growth of crystals in the supersaturated vapour will be possible, but the level of supersaturation may not allow nucleation of crystals. We shall discuss this issue with regards to the nucleation of frost flowers in §4*a*.

3. Linear stability analysis

In the regime diagram, there are two regimes of particular interest. The first of these is regime VI. Here, although the condensed phase is evaporating and the far-field vapour is not supersaturated there is still supersaturation directly above the interface. In this regime, warm vapour evaporating from the condensed phase encounters the cold air above to yield a supersaturated layer lying directly above the surface of the condensed phase. An example of crystal growth in this regime is the appearance of frost flowers on sea ice. Frost flowers are small, hoar-frost-like ice crystals that are commonly found on young sea ice and that have important impacts upon sea-ice albedo (Martin *et al.* 1996) and sea-salt aerosol (Rankin *et al.* 2002) and may be a major factor in tropospheric ozone

depletion (Kaleschke *et al.* 2004). The later stage growth of the frost flowers into the supersaturated vapour can be understood as the growth of a crystal into a supersaturated vapour. However, there remains the important question of whether frost flowers can nucleate from perturbations to the underlying ice, or whether they require a seed crystal to be dropped into the supersaturated layer. We shall address this question in this section by considering the linear stability analysis of the evaporating surface in regime VI. The second regime of interest is given by regime IV in figure 1. In this regime there is condensation from the vapour onto a cold surface, but there is no supersaturation directly above the interface. An example of this regime is the creation of a molecularly rough film by physical vapour deposition, where a substance is vaporized and then condensed onto a cold substrate in order to create crystals with enhanced properties such as hardness and resistance to wear or oxidation (Mahan 2000). A crucial element of creating regular crystals by vapour deposition is ensuring that the surface does not undergo a morphological instability during growth so that irregular, dendritic or cellular crystal growth can be avoided. Reed & LaFleur (1964) argued that the instability will coincide with the presence of supersaturation at the interface, implying that the whole of region IV will be stable. However, we show here that a linear stability analysis of the system implies that the interface is actually stable only in a small region of regime IV.

(*a*) *Model*

In order to consider the linear stability of solid underlying a vapour, we need to move into a different frame of reference so that we can calculate the stability of a perturbation imposed upon a steadily propagating interface. Therefore, we shall consider the system of a pure solid underlying a vapour/air mix shown in figure 4. In order to focus on the instability caused by changes in vapour conditions at the surface, we shall ignore effects such as dislocations, lattice effects and attachment kinetics and concentrate on the case of the growth or evaporation of a molecularly rough crystal (Louchev 1994). We take the solid as being of initial thickness d_s, with the base of the solid being held isothermal at temperature T_2. In the case of frost flower growth on young sea ice, the base of the solid corresponds to the ice–water interface. In the case of crystal growth by vapour deposition the base of the solid corresponds to the interface between the growing crystal and an underlying substrate of high thermal conductivity. The air above the interface is assumed to be in a layer of constant thickness d_a, and the temperature T_1 and vapour density ρ_1 at the top of the layer are taken as constant. During crystal growth by vapour deposition this can correspond either to the vapour release point above the substrate or to the top of a stagnant boundary layer above the crystal such as that observed experimentally to be present by Eversteijn *et al.* (1970). During frost flower growth, buoyancy-driven convection in the air caused by the temperature difference between the ice and the air leads to thermal turbulence above the warm ice. Owing to the viscosity of the air adjacent to the ice, there exists a thin laminar boundary layer that underlies the turbulent, mixed region (Howard 1964). The 'lid' of the system corresponds to the top of the laminar region. During steady-state growth, the planar interface has a fixed temperature T_0, while the vapour density immediately above the interface is ρ_0.

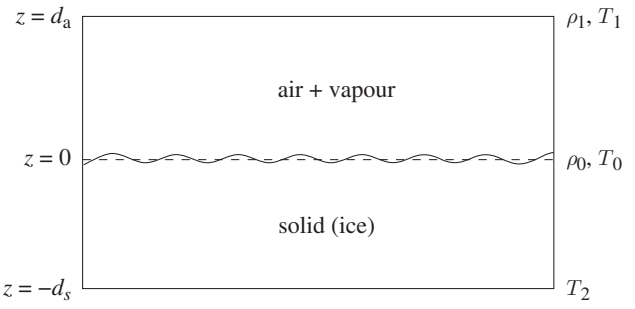

Figure 4. Schematic showing the model used in the stability analysis at a condensing/evaporating interface. Constant temperature and water vapour boundary conditions, respectively, $T = T_1$ and $\rho = \rho_1$, are applied at $z = d_a$ and a constant temperature boundary condition $T = T_2$ is applied at $z = -d_s$. Vapour density ρ_0 and temperature T_0 at $z = 0$ correspond to the vapour density and temperature system with an unperturbed interface.

The temperature and vapour fields satisfy the two-dimensional forms of the advection–diffusion equations (2.1)–(2.3) with the velocities u_0, v_0 being replaced by $\mathbf{v}$ and $\mathbf{u}$, which are the velocity fields in the air and solid relative to the unperturbed ice–air interface. If we scale lengths by the vapour layer thickness d_a, velocities by $D\rho_0/d_a\rho_s$ from consideration of the condition for conservation of water vapour at the interface (2.9), and times by $d_a^2\rho_s/D\rho_0$, then, with tildes denoting dimensionless variables, these advection–diffusion equations become

$$Pe_\rho \left[\frac{\partial \rho}{\partial \tilde{t}} + \tilde{\mathbf{v}} \cdot \tilde{\nabla}\rho\right] = \tilde{\nabla}^2 \rho, \tag{3.1}$$

$$Pe_{\mathrm{th}}^{\mathrm{a}} \left[\frac{\partial T_{\mathrm{a}}}{\partial \tilde{t}} + \tilde{\mathbf{v}} \cdot \tilde{\nabla} T_{\mathbf{a}}\right] = \tilde{\nabla}^2 T_{\mathrm{a}} \tag{3.2}$$

and

$$Pe_{\mathrm{th}}^{s} \left[\frac{\partial T_s}{\partial \tilde{t}} + \tilde{\mathbf{u}} \cdot \tilde{\nabla} T_s\right] = \tilde{\nabla}^2 T_s. \tag{3.3}$$

The solutal and thermal Péclet numbers are defined by

$$Pe_\rho = \frac{\rho_0}{\rho_s}, \quad Pe_{\mathrm{th}}^{\mathrm{a}} = \frac{\rho_0 D}{\rho_s \kappa_{\mathrm{a}}} \quad \text{and} \quad Pe_{\mathrm{th}}^{s} = \frac{\rho_0 D}{\rho_s \kappa_s}. \tag{3.4}$$

These Péclet numbers represent the ratio of advection to diffusion in each phase and are equivalent to the grouping $u_0 L_0/D_0$ where u_0, L_0 and D_0 are representative velocities, length scales and diffusivities, respectively, for each phase.

The boundary conditions comprise the two-dimensional forms of equations (2.6), (2.7) and (2.9) in addition to the condition for water–vapour equilibrium at the interface (2.8), which is modified to include the saturation vapour density dependence upon curvature as given by the Kelvin equation so that

$$\rho = \rho_{\mathrm{sat}}(T_{\mathrm{a}}, \mathcal{K}_{\mathrm{sa}}) = \rho_0 \frac{T_0}{T_{\mathrm{a}}} \mathrm{e}^{-(ML/R)(1/T_{\mathrm{a}} - 1/T_0)} \mathrm{e}^{\gamma_{\mathrm{sa}} M \mathcal{K}_{\mathrm{sa}}/\rho_s R T_{\mathrm{a}}}, \tag{3.5}$$

where $\gamma_{\rm sa}$ is the solid–air surface tension, and $\mathcal{K}_{\rm sa}$ is the curvature of the solid–air interface. On linearization this becomes

$$\frac{\rho-\rho_0}{\rho_0} = f(T_0)(T-T_0) + \Gamma\mathcal{K}_{\rm sa}, \tag{3.6}$$

where $f(T_0)$ is given by equation (2.28) and the surface tension coefficient is

$$\Gamma = \frac{\rho_0 M\gamma_{\rm sa}}{\rho_s R T_0}. \tag{3.7}$$

This linearization is commonly used in vapour stability calculations (Louchev 1994; Libbrecht 2005) and is equivalent to taking a linear approximation to the saturation curve. As we are concerned only with growth immediately adjacent to the steady-state interface and so over the small temperature range in that region, this is a reasonable approximation.

We make two further approximations. Firstly, we shall consider perturbations to the interface where the wavelength of the perturbation is much smaller than the thickness of the solid or vapour layers. For a perturbation of the form

$$h = \epsilon \mathrm{e}^{\mathrm{i}\alpha x+\sigma t}, \tag{3.8}$$

this means that $d_{\rm a}\alpha \gg 1$ and $d_{\rm a}\alpha \gg 1$.

Secondly, we note that, as $\rho_0 \ll \rho_s$ for all typical substances, each of the Péclet numbers are small. For the case of the ice/water–vapour system this can be seen by consideration of typical values of the parameters as shown in table 1, giving $Pe_\rho = 2.6\times10^{-6}$, $Pe^{\rm a}_{\rm th} = 2.3\times10^{-6}$ and $Pe^{s}_{\rm th} = 9.1\times10^{-5}$. Therefore, we shall assume that $Pe \ll 1$ for each field so that the advection–diffusion equations each reduce to Laplace's equation. From the form of equation (3.6) we choose to scale vapour densities with ρ_0 and temperatures with $f(T_0)^{-1}$ so that $\tilde\rho = (\rho-\rho_0)\rho_0$ and $\tilde t = f(T_0)(T-T_0)$.

The system of governing equations then becomes (dropping tildes)

$$\nabla^2\rho = 0, \quad \nabla^2 T_{\rm a} = 0 \quad \text{and} \quad \nabla^2 T_s = 0, \tag{3.9}$$

with boundary conditions at the interface

$$T_{\rm a} = T_s, \quad \rho = T_{\rm a} + \tilde\Gamma\mathcal{K} \tag{3.10}$$

and

$$\beta\frac{\partial\rho}{\partial\mathbf{n}} = \frac{\partial T_s}{\partial\mathbf{n}} - k\frac{\partial T_{\rm a}}{\partial\mathbf{n}} \quad \text{and} \quad \frac{\partial\rho}{\partial\mathbf{n}} = u_n. \tag{3.11}$$

The externally imposed boundary conditions become

$$\rho(1) = \frac{\rho_1-\rho_0}{\rho_0} \equiv \mathcal{F}, \tag{3.12}$$

$$T_{\rm a}(1) = [T_1 - T_0]f(T_0) \equiv \mathcal{G}_{\rm a} \tag{3.13}$$

and

$$T_s(-d) = [T_2 - T_0]f(T_0) = -\mathcal{G}_s, \tag{3.14}$$

and the dimensionless parameters are

$$\beta = \frac{f(T_0)LD\rho_0}{k_s}, \quad \tilde{\Gamma} = \frac{\Gamma}{d_\mathrm{a}}, \quad d = \frac{d_s}{d_\mathrm{a}} \quad \text{and} \quad k = \frac{k_\mathrm{a}}{k_s}, \tag{3.15}$$

where β is a type of Stefan number, $\tilde{\Gamma}$ is the dimensionless surface tension, d is the ratio of the thickness of the solid and air layers and k is the ratio of thermal conductivities. Note that $\mathcal{F} = (\rho_1 - \rho_0)/d_\mathrm{a}$, $\mathcal{G}_\mathrm{a} = (T_1 - T_0)/d_\mathrm{a}$ and $\mathcal{G}_s = (T_0 - T_2)/d_s$ are the non-dimensional vapour and temperature gradients F_0, G_0^a and G_0^s, respectively.

Steady-state planar growth is given by linear vapour and temperature profiles

$$\rho = \mathcal{F}z, \quad T_\mathrm{a} = \mathcal{G}_\mathrm{a}z \quad \text{and} \quad T_s = \mathcal{G}_s z, \tag{3.16}$$

and, from the boundary conditions for conservation of water vapour and heat, we find that the steady-state growth velocity is given by

$$u_0 = \mathcal{F} \tag{3.17}$$

and

$$\beta\mathcal{F} = \mathcal{G}_s - k\mathcal{G}_\mathrm{a}. \tag{3.18}$$

We can now proceed to perform a linear stability analysis upon this system by adding a small sinusoidal perturbation to the solid–air interface such that the new interface position is given by

$$h = \epsilon \mathrm{e}^{\mathrm{i}\alpha x + \sigma t}. \tag{3.19}$$

We can assume forms for the vapour and temperature fields such that they satisfy Laplace's equation,

$$\rho = \mathcal{F}z + A\epsilon \mathrm{e}^{\mathrm{i}\alpha x + \sigma t} \sinh \alpha(z-1), \tag{3.20}$$

$$T_\mathrm{a} = \mathcal{G}_\mathrm{a}z + B\epsilon \mathrm{e}^{\mathrm{i}\alpha x + \sigma t} \sinh \alpha(z-1) \tag{3.21}$$

and

$$T_s = \mathcal{G}_s z + C\epsilon \mathrm{e}^{\mathrm{i}\alpha x + \sigma t} \sinh \alpha(z+d). \tag{3.22}$$

Then applying the remaining boundary conditions (3.10) and (3.11) and solving for σ, we obtain the dispersion relation

$$\sigma = \frac{(1+k)}{(1+k+\beta)} \left(\mathcal{F} - \frac{(\mathcal{G}_s + \mathcal{G}_\mathrm{a})}{(1+k)} - \tilde{\Gamma}\alpha^2 \right) \alpha, \tag{3.23}$$

where we have used the previously mentioned assumption that the wavelength of the instability is much smaller than the thickness of either solid or vapour layers, so that $\alpha \ll 1$ and $\alpha d \ll 1$. This dispersion relation takes a similar form to the dispersion relation for the Mullins–Sekerka instability in binary alloys (Mullins & Sekerka 1964), but importantly contains different parameters that take account of the difference between vapour systems and the solidification problem. These parameters are important to know in understanding the characteristics of instability at a solid–vapour interface.

(*b*) *Results*

Equation (3.23) gives a dispersion relation for small perturbations of the system. From this we can calculate the neutral stability curve that separates parts of the regime diagram where unstable wavelengths exist, from parts where all wavelengths are linearly stable. By use of equation (3.18) we find that the neutral stability curve is given by

$$\mathcal{F} = \frac{2k}{1+k-\beta}\mathcal{G}_{\mathrm{a}}. \tag{3.24}$$

This corresponds to the vapour gradient above which the interface will be morphologically unstable.

At this point, we note that Louchev (1994) has previously performed a linear stability analysis for physical vapour deposition of films. However, in that analysis it was assumed that the conduction of heat in the air was negligible compared with that in the solid, and so was ignored in the condition for conservation of heat at the interface (3.11). From equation (3.23) it can be seen that this approximation leads to system stability when $\mathcal{F} < \mathcal{G}_s/(1+k) \approx \mathcal{G}_s$ as the ratio of conductivities k is small for typical materials. However, by eliminating $\mathcal{G}_s$ from equation (3.24) by use of equation (3.18), we find that the system is actually stable when

$$\mathcal{F} < \frac{2}{1+k+\beta}\mathcal{G}_s \approx 2\mathcal{G}_s. \tag{3.25}$$

We can see that, despite the small conductivity ratio k, the large temperature gradients in the air relative to those in the solid mean that heat conduction in the air is still large enough to influence the stability of the interface significantly.

We can relate the neutral stability curve to the regime diagram in figure 1 by expressing equation (3.24) in terms of $\rho_1/\rho_{\mathrm{sat}}(T_1)$, T_0 and T_1, and replacing T_∞ by T_1 in the regime diagram. This gives

$$\frac{\rho_1}{\rho_{\mathrm{sat}}(T_1)} = \frac{T_1}{T_0}\left(1 + 2kf(T_0)\frac{T_1 - T_0}{1+k-\beta}\right)\mathrm{e}^{-(ML/R)(1/T_0 - 1/T_1)}, \tag{3.26}$$

and in the common case that the reduced temperature $\tau = (T_1 - T_0)/T_1 \ll 1$, this reduces to

$$\frac{\rho_1}{\rho_{\mathrm{sat}}(T_1)} = \left[1 + \left(\frac{1-\beta-k+2km}{1+k-\beta}\right)\tau\right]\mathrm{e}^{-m\tau}. \tag{3.27}$$

Figure 5 shows the results of the linear stability analysis as given by equation (3.26) when added to the regime diagram (figure 1). Both figures use typical parameters for the ice/water–vapour system as shown in table 1 and a range of values of the dimensionless parameter k. Figure 5*a* shows the results when $T_1 < T_0$, while figure 5*b* shows the results when $T_1 > T_0$. It can be seen that, for realistic values of k (approx. 0.01), the neutral stability curve is very close to the curve separating condensation and evaporation. Interestingly, it can be seen in figure 5*a* that the surface can be stable despite the presence of supersaturation above the interface during evaporation. Conversely, figure 5*b* shows that during condensation it is possible for instability of the surface to occur despite the air above the surface being unsaturated.

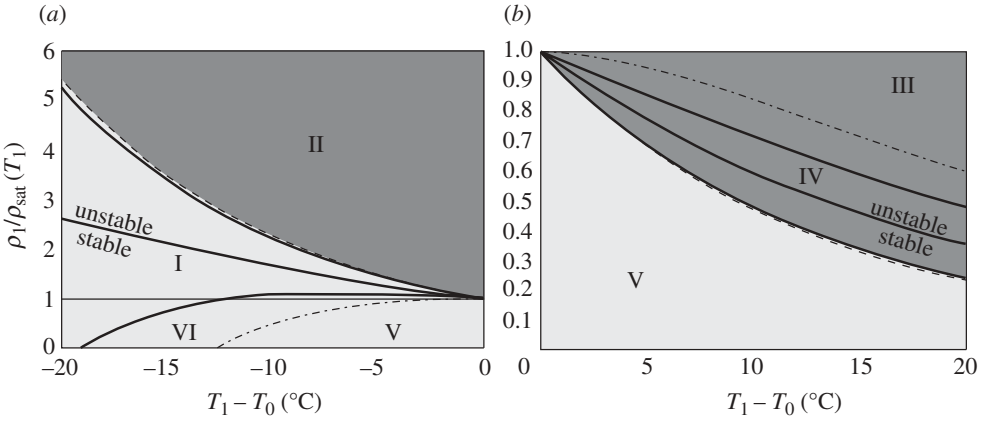

Figure 5. The dimensional neutral stability curves included in figure 1. Regime boundaries are given by the dashed and dash-dotted curves and the continuous line (corresponding to 100% relative humidity of the far-field vapour). (*a*) Continuous curves from top to bottom correspond to neutral curves for $k = 0.01$, $k = 0.2$, $k = 0.5$ when $T_1 < T_0$. (*b*) Curves for the same values of k when $T_1 > T_0$. The order is reversed so that the lowest curve corresponds to $k = 0.01$. As $k \to 0$, the neutral stability curve approaches the curve delineating between evaporation and condensation regimes. In each case, the interface is linearly stable below the neutral curve, and linearly unstable (over at least a range of wavenumbers) above the neutral curve.

4. Discussion

(*a*) *Regime VI: frost flowers*

On dimensionalization of the neutral stability condition (3.24), and using equation (3.18) we find that

$$F_0 < \frac{\partial \rho_{\mathrm{sat}}}{\partial T}\left(\frac{k_s G_0^s + k_{\mathrm{a}} G_0^{\mathrm{a}}}{k_s + k_{\mathrm{a}}}\right), \tag{4.1}$$

where F_0 is the dimensional vapour-density gradient $(\rho_1 - \rho_0)/d_{\mathrm{a}}$. This physically expresses the fact that perturbations to the interface will experience a conductivity-weighted temperature gradient during growth given by

$$G_{\mathrm{m}} = \frac{k_s G_0^s + k_{\mathrm{a}} G_0^{\mathrm{a}}}{k_s + k_{\mathrm{a}}} \tag{4.2}$$

(cf. the Mullins–Sekerka instability (Mullins & Sekerka 1964)). This 'apparent' temperature gradient can be modified substantially from the temperature gradient in the air by conduction of heat in the solid. Because of this effect, it can be seen from figure 5*a* that, in typical frost flower growth conditions (regime VI), the surface is linearly stable despite the presence of supersaturation directly above the interface.

Although the surface is linearly stable to perturbations, perturbations of sufficiently high aspect ratio will grow by condensation from the supersaturated layer. This can be demonstrated by consideration of a tall, thin needle-like perturbation to the interface which we take to be a cylinder of height h and

radius r, where $h \gg r$. Heat conduction from the underlying ice will be through the base of the cylinder and take the form

$$H_h = k_s \frac{\partial T}{\partial z} \pi r^2 \sim \pi k_s r^2 \frac{\Delta T}{h}, \tag{4.3}$$

where ΔT is the temperature difference between the ice and the air. Cooling of the cylinder will occur owing to heat conduction in the air and assuming a boundary layer of thickness r around the cylinder; the cooling can be estimated by

$$H_c = k_a \frac{(T - T_a)}{r} 2\pi rh \sim 2\pi k_a rh \frac{\Delta T}{r}. \tag{4.4}$$

In order for the tip of the cylinder to be at the surrounding air temperature as it grows into the supersaturated vapour, the heating from underlying ice must be small in comparison with cooling from the air so that $H_c \gtrsim H_h$, which gives that

$$\frac{h}{r} \gtrsim \sqrt{\frac{k_s}{2k_a}}. \tag{4.5}$$

In the case of the ice/water–vapour system (with parameters given in table 1), this means that, for a perturbation to grow into the supersaturated vapour above an evaporating surface such as found in regime VI, the perturbation must have an aspect ratio greater than about 7.

On sea ice, where frost flowers grow naturally, the surface of the ice is covered in a brine film which will tend to engulf such high aspect ratio perturbations. This means that nucleation of frost flowers from the underlying sea ice is unlikely to be caused by an instability of the surface into the adjacent supersaturated vapour. However, if a foreign particle were to land on the ice surface in a manner so that the particle was in poor thermal contact with the ice (or if the particle were sufficiently ramified so that heat was poorly conducted to the exposed tips of the particle), ice can then condense onto the particle from the supersaturated layer. In polar regions, there is a plentiful supply of atmospheric particles that could drop onto the sea-ice surface to nucleate frost flowers. Snowflakes, for example, are ramified structures and so would serve as an ideal nucleus for a frost flower. Diamond dust and clearsky ice crystals are also commonly observed in polar regions, originating in regions with abundant sources of vapour (such as the open leads commonly associated with frost flower growth; Ohtake *et al.* 1982). According to Girard & Blanchet (2001), diamond dust has been shown to fall between 20 and 50 per cent of the time in the arctic wintertime, though these frequencies may be underestimated owing to the difficulties of observation in the winter darkness. Data are also given showing typical particle sizes varying between a few microns and several hundred microns, with number concentrations of between 1 and 1000 particles per litre of air. Therefore, these particles are sufficiently large and abundant to act as possible frost flower nuclei and we suggest that a possible method of nucleation of frost flowers other than surface instability is that of heterogeneously nucleated growth from atmospheric ice crystals landing on the evaporating ice surface. Importantly, this also explains the observation of frost flower 'patches' whereby frost flowers appear initially in isolated sites which grow laterally across the surface (Martin *et al.* 1995). In experimental growth of frost flowers, we have observed turbulence

from the cooling fans blowing hoar frost from the tank sides onto the ice surface, nucleating frost flower patches, and this observation would appear to substantiate this idea.

(*b*) *Regime IV: crystal growth by vapour deposition*

Figure 5*b* shows when instability occurs for the ice/water–vapour system where the ice is colder than the surrounding air. It can be seen that, for $k = 0.01$, the curve separating stable and unstable conditions is close to the boundary between condensation and evaporation. This means that in regime IV, despite the fact that there is no supersaturation above the surface, there is only a narrow range of parameters for which condensation occurs without surface instability. The cause of the instability is the fact that perturbations to the ice surface growing up into the warm air are cooled by the high thermal conductivity of the underlying solid. The warm, moist air directly surrounding the peaks of the perturbations is then cooled, becoming supersaturated, and leading to further growth of the perturbation.

From the linear stability analysis, we can calculate the maximum stable growth rate for a vapour-grown crystal. By dimensionalization of equation (3.24), we find that the system is stable when

$$F_0 > \frac{2\rho_0 f(T_0) k}{1 + k - \beta} G_0^{\mathrm{a}}, \tag{4.6}$$

and by using the dimensional form of equation $(3.11)_2$, we find that the maximum velocity of stable growth is given by

$$u = \frac{2D\rho_0 f(T_0) k}{\rho_s (1 + k - \beta)} G_0^{\mathrm{a}}. \tag{4.7}$$

For a typical ice/water–vapour system, $k, \beta \ll 1$ and so the maximum stable growth velocity can be approximated by

$$u_{\max} = 2\frac{\rho_0}{\rho_s} D f(T_0) k G_0^{\mathrm{a}}. \tag{4.8}$$

Equation (4.8) demonstrates the key importance of the system temperature gradient in maintaining stability of growth, as the maximum stable growth velocity can be seen to be limited only by the temperature gradient across the layer of air above the crystal. It also shows the strong dependence of stability upon vapour diffusivity D, vapour density at the interface ρ_0 and the ratio of thermal conductivities $k = k_{\mathrm{a}}/k_s$.

This result is different from the result of Reed & LaFleur (1964), who assumed that instability occurred as soon as the vapour above the solid crystal was supersaturated. This would imply that the maximum stable growth rate is

$$u_{\max} = \frac{D\rho f(T_0)}{\rho_s} G_0^{\mathrm{a}}. \tag{4.9}$$

This velocity is larger than the predicted velocity arising from the stability analysis by a factor of $1/2k$. This means that for the ice–vapour system the maximum growth value according to Reed & LaFleur (1964) is approximately a factor of 50 times larger.

In this analysis, we have ignored factors such as attachment kinetics, dislocations and lattice effects in order to concentrate on the instability mechanism. Therefore, this maximum growth velocity is appropriate for a molecularly rough crystal growing into its vapour, and may differ when these other effects occur. However, even in the presence of these effects, this model provides valuable insight into the process controlling the instability. It also demonstrates the leading role played by the temperature gradients in both the solid and vapour phases. It shows that, despite the small temperature gradient in the solid and the small thermal conductivity of the air, both temperature gradients have a leading order effect upon the stability of the surface and so neither can be neglected.

5. Conclusions

In this paper, we have solved a planar model for a condensed phase in contact with its vapour and analysed the stability of a solid crystal in contact with its vapour. First, we presented the equations relevant to condensation onto, or sublimation (evaporation) from, a condensed phase in contact with its vapour. We have solved these equations and shown that there exist similarity solutions for the evolution of the temperature and vapour profiles. We have used these profiles to demonstrate a new condition for supersaturation when the vapour and solutal diffusivities in the air are not equal. In the case that the reduced temperature $\tau = (T_\infty - T_0)/T_\infty$ is small, this condition is given by

$$\frac{\rho_\infty}{\rho_{\mathrm{sat}}(\infty)} > \mathrm{e}^{-m\tau}\left[1 + \tau\left(1 + m\sqrt{\frac{D}{\kappa_{\mathrm{a}}}} - \sqrt{\frac{D}{\kappa_{\mathrm{a}}}}\right)\right].$$

In addition, we have calculated profiles to illustrate vapour characteristics in the different regimes of the regime diagram shown in figure 1. Eight profiles were calculated for a typical ice–vapour system, with four profiles being calculated in the case of a cold condensed phase underlying warm air for varying far-field densities, and four profiles calculated in the case of a warm condensed phase underlying cold air for varying far-field densities. These profiles, shown in figure 3, show typical characteristics found in each of the regimes in the regime diagram.

The results of the linear stability analysis of the solid/vapour system show that there is surface instability when the gradient of vapour density above the interface satisfies

$$F_0 < \frac{\partial \rho_{\mathrm{sat}}}{\partial T}\left(\frac{k_s G_0^s + k_{\mathrm{a}} G_0^{\mathrm{a}}}{k_s + k_{\mathrm{a}}}\right).$$

In the case of frost flower growth in regime VI, we have shown that for typical frost flower growth conditions the sea-ice surface will be linearly stable to perturbations, despite the presence of a supersaturated layer of vapour directly above it. We have demonstrated that it is possible for instabilities of sufficiently high aspect ratio (greater than approx. 7) to nucleate frost flower growth from the vapour. However, formation of such crystals is unlikely as the brine film in the interstices of sea ice will tend to engulf such crystals. We suggest that a source of frost flower nucleation is the falling of atmospheric ice crystals onto

young sea ice as these ice crystals are common in polar regions (especially near leads). Heterogeneous nucleation also explains observations that frost flowers are initially dry but become wetted by capillarity when they come into contact with brine in the underlying sea ice (Domine *et al.* 2005), as instabilities growing directly from the sea ice would be likely to be brine covered throughout the growth process. Understanding this growth process raises the possibility of producing an equation describing the areal coverage of frost flowers based on nucleation rate and atmospheric conditions.

In the case of crystal growth by vapour deposition, we have shown that instability of the crystal surface will occur during condensation growth despite the lack of a supersaturated layer of vapour directly above the crystal if the growth velocity of the crystal exceeds the maximum stable growth velocity

$$u_{\max} = \frac{2D\rho_0 f(T_0)k}{\rho_s(1+k-\beta)} G_0^{\mathrm{a}}.$$

In order to grow crystals without instability, the crystals must be grown in the narrow parameter regime shown in figure 5*b* beneath the neutral stability curve (the lowermost, thin, continuous line) and in the region of condensational growth (dark grey shaded). The expression for the maximum crystal growth velocity demonstrates that this figure is limited by the temperature gradient in the vapour above the interface and strongly influenced by the vapour diffusivity, vapour density and the ratio of the thermal conductivities. The analysis also shows that the temperature gradients in both solid and vapour phases play a leading order role in determining the stability of the interface and so neither can be neglected, as has been previously assumed.

This work is applicable to many phenomena involving condensation or evaporation of a solid phase, in particular to the many instances of ice crystal growth such as rime, hoar frost, depth hoar and jack frost. The extension of the regime diagram to general solid–vapour systems means that this analysis should help in understanding the wide variety of situations that arise in solid–vapour interactions.

This work was supported by a Case studentship from the Natural Environment Research Council in collaboration with the British Antarctic Survey.

References

Deegan, R. D., Bakajin, O., Dupont, T. F., Huber, G., Nagel, S. R. & Witten, T. A. 2000 Contact line deposits in an evaporating drop. *Phys. Rev. E* **62**, 756–765. (doi:10.1103/PhysRevE.62.756)

Domine, F., Taillandier, A. S., Simpson, W. R. & Severin, K. 2005 Specific surface area density and microstructure of frost flowers. *Geophys. Res. Lett.* **32**, L13502. (doi:10.1029/2005GL023245)

Eversteijn, F. C., Severin, P. J. W., van den Brekel, C. H. J. & Peek, H. L. 1970 A stagnant layer model for the epitaxial growth of silicon from silane in a horizontal reactor. *J. Electrochem. Soc.* **117**, 925–931. (doi:10.1149/1.2407685)

Girard, E. & Blanchet, J.-P. 2001 Microphysical parameterization of arctic diamond dust, ice fog, and thin stratus for climate models. *J. Atmos. Sci.* **58**, 1181–1198. (doi:10.1175/15200469(2001)058<1181:MPOADD>2.0.CO;2)

Howard, L. N. 1964 Convection at high rayleigh number. In *Proc. Eleventh Int. Congr. of Applied Mechanics. Munich, Germany* (ed. H. Görtler), pp. 1109–1115. Berlin, Germany: Springer.

Kaleschke, L. *et al.* 2004 Frost flowers on sea ice as a source of sea salt and their influence on tropospheric halogen chemistry. *Geophys. Res. Lett.* **31**, L16114. (doi:10.1029/2004GL020655)

Libbrecht, K. G. 2005. The physics of snow crystals. *Rep. Prog. Phys.* **68**, 855–895. (doi:10.1088/0034-4885/68/4/R03)

Louchev, O. 1994 Diffusion, heat transfer, equilibrium molecular density and kinetic mechanism of morphological instability in physical vapor deposition. *J. Cryst. Growth* **140**, 219–236. (doi:10.1016/0022-0248(94)90516-9)

Mahan, J. E. 2000 *Physical vapor deposition of thin films*. New York, NY: Wiley.

Martin, S., Drucker, R. & Fort, M. 1995 A laboratory study of frost flower growth on the surface of young sea ice. *J. Geophys. Res* **100**, 7027–7036. (doi:10.1029/94JC03243)

Martin, S., Yu, Y. & Drucker, R. 1996 The temperature dependence of frost flower growth on laboratory sea ice and the effect of the flowers on infrared observations of the surface. *J. Geophys. Res.* **101**, 12 111–12 126. (doi:10.1029/96JC00208)

Mullins, W. W. & Sekerka, R. F. 1964 Stability of a planar interface during solidification of a dilute binary alloy. *J. Appl. Phys.* **35**, 444. (doi:10.1063/1.1713333)

Ohtake, T., Jayaweera, K. & Sakurai, K. 1982 Observation of ice crystal formation in lower arctic atmosphere. *J. Atmos. Sci.* **39**, 2898–2904. (doi:10.1175/1520-0469(1982)039<2898:OOICFI>2.0.CO;2)

Rankin, A. M., Wolff, E. W. & Martin, S. 2002 Frost flowers: implications for tropospheric chemisty and ice core interpretation. *J. Geophys. Res.* **107**, 4683. (doi:10.1029/2002JD002492)

Reed, T. B. & LaFleur, W. J. 1964 Constitutional supercooling in iodine vapor crystal growth. *Appl. Phys. Lett.* **5**, 191–193. (doi:10.1063/1.1723583)

Style, R. W. & Wettlaufer, J. S. 2007 Evaporatively driven morphological instability. *Phys. Rev. E.* **76**, 011602. (doi:10.1103/PhysRevE.76.011602)

Style, R. W. & Worster, M. G. 2009 Frost flower formation on sea ice and lake ice. *Geophys. Res. Lett.* **36**, L11501. (doi:10.1029/2009GL037304)

Wood, S. E. & Battino, R. 1990 *Thermodynamics of chemical systems*. Cambridge, UK: Cambridge University Press.

Worster, M. G. 2000 Solidification of fluids. In *Perspectives in fluid dynamics* (eds G. K. Batchelor, H. K. Moffat & M. G. Worster). Cambridge, UK: Cambridge University Press.